Supplementary Information: Epitaxial Pb on InAs nanowires

Thomas Kanne,[*,†] Mikelis Marnauza,[†] Dags Olsteins,[†] Damon J. Carrad,[†] Joachim E. Sestoft,[†] Joeri de Bruijckere,[†,¶] Lunjie Zeng,[‡] Erik Johnson,[†] Eva Olsson,[‡] Kasper Grove-Rasmussen,[†] and Jesper Nygård[†]

†*Center For Quantum Devices, Niels Bohr Institute, University of Copenhagen, 2100 Copenhagen, Denmark*

‡*Department of Applied Physics, Chalmers University of Technology, Gothenburg, Sweden*

¶*Kavli Institute of Nanoscience, Delft University of Technology, 2628 CJ Delft, The Netherlands*

E-mail: thomas.kanne@nbi.ku.dk

Contents

1 Thin film growth on nanowires **3**
1.1 Single element growth evolution . . . 3
1.2 Controlling Pb thin film growth . . . 7
1.3 Controlling Al thin film growth . . . 10

2 Finding optimal single element materials for large-grain heteroepitaxial growth **11**
2.1 Aluminium . . . 13
2.2 Thallium . . . 14
2.3 Indium . . . 14
2.4 Tin . . . 15

3 Pb epitaxy **16**
3.1 InAs/Pb epitaxy . . . 17
3.2 Other semiconductors/Pb . . . 20

4 Additional transport data **22**
4.1 Spectroscopy on half-shell InAs/Pb nanowires. . . . 22
4.2 Coulomb spectroscopy on InAs/Pb islands . . . 23
4.2.1 InAs/Pb island in perpendicular magnetic fields . . . 23
4.2.2 Analysis of the Coulomb-peak spacings . . . 24
4.3 Tunnel spectroscopy on full-shell InAs/Pb nanowires . . . 26

5 Processing Pb coated InAs nanowires for devices **28**

References **29**

In the following we present supplementary information related to the article *Epitaxial Pb on InAs nanowires.* In section 1 thin film growth on nanowires is adressed. Here the first part (1.1) analytically discuss fundamental aspects of single element heteroepitaxial growth on faceted nanowires. We focus on experimental observations and utilize classical nucleation theory to highlight some of the most important control parameters. The analytical considerations are used to optimize the morphology and crystal orientation of Pb and Al films in section 1.2 and 1.3, respectively. These considerations are used in section 2 as a conceptual background to showcase materials that would potentially allow for large grain heteroepitaxial interfaces on different semiconducting nanowires. In section 3 Pb epitaxy on InAs nanowires is discussed in more detail alongside suggestions of other possible III-V semiconductor/Pb combinations. In section 4 we provide extended transport data on the measured devices. Lastly, section 5 provides an overview of how to handle Pb for device fabrication.

1 Thin film growth on nanowires

Thin metal film formation typically proceeds through a series of nucleation and grain growth stages that are governed by an interplay between thermodynamic driving forces and kinetically limiting processes[1]. The outcome is commonly non-equilibrium structures in terms of crystal grain size and morphology. This is primarily due to a limited experimental temperature range and because thermodynamic equilibrium rarely promotes a thin continuous film. As an example, in-situ deposition of materials on InAs nanowires should be kept below a substrate temperature of 200 C to prevent undesired alloy formation at the interface [2]. The experimental setup similarly caps the lower substrate temperature (the system used for present experiments cannot go lower than $T_{sub} \sim 120$ K). As previously shown in ref. [3] in-situ deposited Al on InAs nanowires at elevated substrate temperatures forms a non-continuous and dewetted film. This is similarly shown for Pb in section 1.2.

1.1 Single element growth evolution

A physical vapor deposition technique (PVD), such as electron beam evaporation, is used to deposit atoms onto the substrate. These atoms (in the vapour phase) initially have an average kinetic energy of $\frac{3}{2}k_b T_{source}$ before they get trapped by the surface potential [4]. This energy is transferred to the substrate after a few lattice vibrations [4] and therefore ignored in this simple description, under the assumption of negligible influence on the substrate temperature. We note that some physical vapour deposition techniques may irradiate heat from the evaporation source and thus transfer heat to the substrate relative to the refractivity of the substrate. This is also ignored, however, it may be controlled by the choice of PVD technique or choice of e.g. evaporation crucible. The atoms on the substrate (adatoms) may surmount the adsorption potential and diffuse on the substrate with an average displacement of $\bar{x} = \sqrt{D\tau}$ [5, 6]. Here D is the diffusion constant which is given by $D = D_0 \exp\left(\frac{-E_d}{k_b T_{sub}}\right)$, where the constant $D_0 = a^2\nu$. a^2 , ν and τ are the distance between surface potential sites, adatom vibrations frequency and average life time before the adatom is either joining a cluster or desorbing, respectively. E_d is the activation energy of diffusion and describes free

energy change between the equilibrium “trapped” position and the height of the substrate potential. Density functional theory simulations suggest that E_d approximately scales as one sixth of the bulk cohesive energy (bulk binding energy) [5] whereas experimental investigation ties the activation energy together with the melting temperature[7].

When the adatoms diffuse on the substrate they may interact and form small nucleation clusters. This process is reversible up to a certain point where a specific critical cluster size is reached. The Gibbs free energy change (ΔG) of such a cluster as function of the amount of atoms in the cluster, j, can be described as [6]

$$\Delta G(j) \sim -j\Delta\mu + j^{2/3}\sum_m C_m\gamma_m. \tag{1}$$

Here μ is the change in chemical potential from either vapour, in the case of direct impingement, or from adatoms being bound in the cluster. This energy change may, for bigger clusters, be proportional to the condensation energy. $\sum_m \gamma_m$ is the sum of surface and interface energies where C_m is a geometric constant related to j. This simple expression for the formation (nucleation) of the initial clusters consists of two terms: a gain in energy from cluster formation and a loss in energy from surfaces. It can be simplified to $\Delta G(j) = E_{gain}(j) - E_{loss}(j)$.

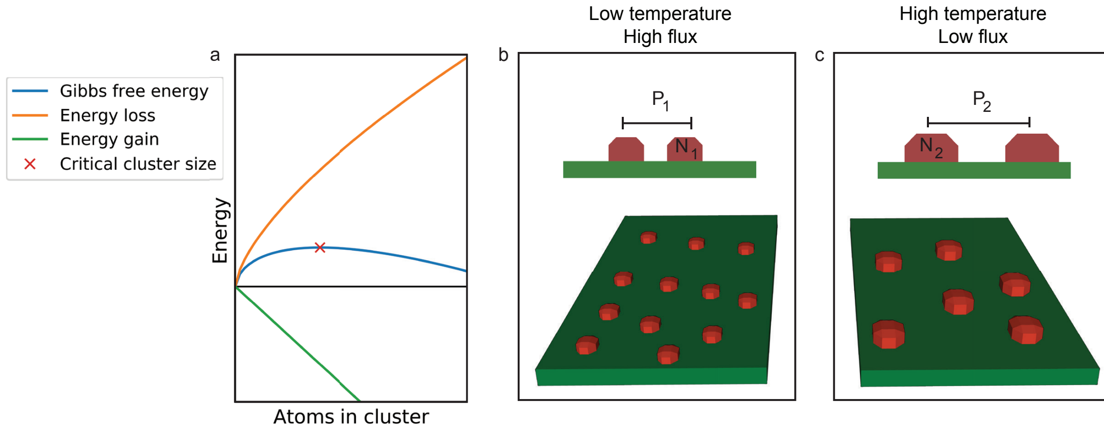

Figure S1: Initial cluster size and pitch depending on substrate temperature and adatom flux. **a** Gibbs free energy as a function of cluster size. **b** Low substrate temperature and high adatom flux results in small clusters. **c** High substrate temperature and low adatom flux results in large initial clusters.

In Fig. S1 **a** the change of Gibbs free energy, energy gain and loss as a function of the number of atoms in the cluster are shown. Here the gain in energy scales linearly with the amount of atoms whereas the loss scales as $j^{2/3}$. However, it is known that this is a rough approximation as in real systems the binding and surface energy commonly relate to the size of the cluster [1, 8] . From Eq. 1 a critical cluster size is reached when [6]

$$\Delta G(i) \sim \frac{4}{27}\frac{\left(\sum_m C_m\gamma_m\right)^3}{\left(\Delta\mu\right)^2}, i \sim \left(\frac{2\sum_m C_m\gamma_m}{3\Delta\mu}\right)^3 \tag{2}$$

and indicated by a red cross in Fig. S1 **a**. Thermal fluctuations (k_bT_{sub}) may induce a spread in critical cluster size which is generally given as the reciprocal of the non-equilibrium Zeldovich factor [1]. Recent studies have shown that at sufficiently low temperatures critical clusters may be energetically stable even if they contain few atoms. Because of this the adatom mobility has in previous reports been discussed as the main phenomenological mechanism that determines the initial cluster size and inter-cluster spacing. Under the assumption of negligible incorporation of adatoms into the substrate, the density of stable clusters (n_x) in a steady state regime is found to be [9]

$$n_x \sim \left(\frac{F}{D}\right)^{\frac{i}{i+2}} \exp\left(\frac{-E_b}{(i+2)k_bT}\right) \tag{3}$$

Here F is the flux of incoming material, D is the aforementioned diffusion constant and E_b is the binding energy of a critical cluster with i atoms (For more information see ref. [10]).

In Fig. S1 **b** and **c** the consequences of eq. 3 are schematically shown. Here a single element material is deposited with either a higher/lower flux and/or with a higher/lower substrate temperature. The amount of atoms in a critical cluster i can be approximated by eq. 1, however recent investigations have found that i also scales with temperature [9, 11]. This may be explained via the spread in critical cluster size due to thermal fluctuations, i.e. the Zeldovich factor. The morphology and crystal orientation of the initial clusters is determined by minimization of the overall excess energy, eq. 1. In the case of crystalline clusters that are not attached to other clusters the contribution is mainly from interface, surface and strain energies. As the clusters grow beyond their critical size, the minimum crystal phase energy may be minimized with another morphology or crystal orientation. Thus the thermodynamic driving force can be summarized in four terms as

$$\Delta E_{drive} = \Delta E_{surface} + \Delta E_{interface} + \Delta E_{strain}\left(+ \Delta E_{GB}\right)$$

where the grain boundary energy (E_{GB}) only contributes to the overall excess energy for impinging clusters. If the thermodynamic driving forces are large enough to overcome the kinetic barrier for recrystallization (related to the cluster binding energy) the cluster may then recrystallize into the lower grain phase energy configuration, see Fig. S2 **a**.

In Fig. S2 **a** two different scenarios are presented. Here different sized initial clusters are depicted with N_1 and N_2 single element atoms, their crystal orientation relative to the substrate is shown by the black arrow. The initial cluster containing N_1 atoms is able to recrystallize into a lower crystal phase energy orientation as it grows whereas the bigger cluster initially containing N_2 atoms is kinetically forced to stay in the higher energy crystal phase orientation. This simple schematic is used to illustrate how the size of the initial clusters may influence the orientation of the clusters in the later stages. As the clusters grow even more, they begin to interact. This generally influences restructuring processes that

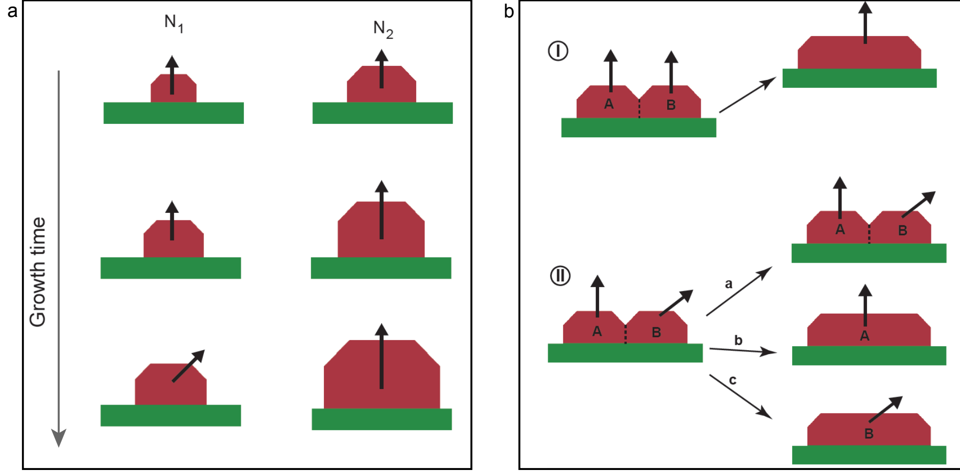

Figure S2: **a** Crystal orientation relative to the growth substrate is depicted with a black arrow and depends on the amount of atoms in the cluster (N). As the initial clusters ($N_1 < N_2$) grow as function of time the crystal orientation may change depending on the thermodynamic driving forces and the kinetic barriers (dependent on N). **b** Recrystallization process for two impinging clusters. (I) Initial clusters with the same crystallographic orientation merge by retaining their crystallographic orientation. (II) Clusters with different crystallographic orientations upon merging are able to undergo recrystallization by either (a) not changing their crystallographic orientation or (b-c) by adapting crystallographic orientation of either cluster A or B.

aim to minimize the energy. Depending on the surface energies, impinging clusters deform elastically and form a grain boundary [12–14]. As a rule of thumb one can approximate the average random grain boundary energy as 0.3 times the free surface energy [15].

Impinging clusters may recrystallize into one single crystal in order to minimize their collective overall excess energy via two different routes, as depicted in Fig. S2 **b**. If the two crystals (A,B) have the same crystallographic orientation they will merge into one by either rearranging the cluster atoms or by the flux of deposited atoms (adatoms) as schematically illustrated in Fig. S2 **b**-I. This processes is generally characteristic for clusters with a discrete and low surface-grain interface energy. The second route involves two clusters with two different crystallographic orientations, as schematically shown in Fig. S2 **b**-II. The grain boundary between the two clusters is able to migrate, thus recrystallizing either cluster A or cluster B. The migration rate (v) of the grain boundary is controlled by the grain boundary mobility (m) and a thermodynamic driving force for crystallization (p), $v = mp$ [13]. The motion of the grain boundary is a thermally activated process given by $m = m_0 \exp(-H/k_bT)$. Here H is the activation enthalpy of grain boundary migration and m_0 is the mobility factor. The grain boundary mobility is strongly dependent on the crystallographic misalignment between the grains. As depicted in Fig S2 **b**-II, the grain boundary may be immobile (a) if the thermodynamic driving force for recrystallizing is not sufficient to overcome the grain boundary kinetic mobility barrier. On the other hand, if it is large enough a recrystallization process may form a single crystal, either by recrystallizing crystal B (b) or crystal A (c).

1.2 Controlling Pb thin film growth

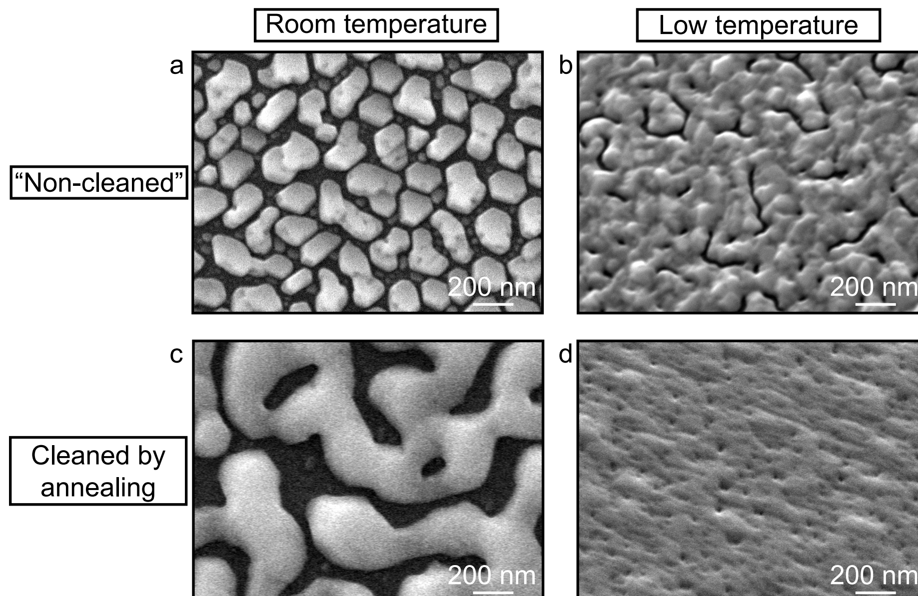

Figure S3: Scanning electron microscope micrographs of Pb thin films deposited onto InAs $[11\bar{2}]$ substrates. **a-b** 20 nm Pb thin film deposited at room temperature and ~ -150 C, respectively. **c-d** 20 nm Pb thin film deposited at room temperature and ~ -150 C, respectively, on substrates which have been in-situ degassed under high temperatures in As_2 overpressure.

Thin films of Pb (20 nm) were deposited onto a series of InAs $(11\bar{2})$ substrates at different conditions to investigate Pb thin film morphology. The crystallographic orientation of the substrate was chosen in order to represent a Zinc Blende (ZB) InAs nanowire facet, which is similar to a $\{1\bar{1}00\}$ WZ InAs facet. The Pb thin film was first deposited at room temperature under ultra high vacuum, see Fig. S3 **a**. Here faceted islands were observed and the film was generally found to be non-continuous. The six-fold facets perpendicular to the substrate indicate that the islands attain a low surface energy with the $\{111\}$ out of plane orientation. In Fig. S3 **c** the substrate was first annealed at 610 C for 20 min under As_2 overpressure before depositing the Pb film at room temperature. This step was implemented to reduce the amount of surface contamination. Here the Pb film morphology is observed to be less faceted with a labyrinthic semi-continuous structure. By cooling to $T_{sub} \sim 120$ K with a substrate that is not annealed before deposition, the film appears almost continuous, however, morphologically rough with cracks as seen in Fig. S3 **b**. By implementing the annealing step prior to the in-situ deposition at low temperature the thin Pb film appeared continuous with small pinholes, as seen in Fig. S3 **d**.

From Fig. S3 it is evident that the substrate surface cleanliness greatly improves the Pb film morphology. As described in section 1.1 the choice of substrate has a large influence on the morphology, crystal grain size, and grain orientation. By cleaning the substrate the average adatom displacement can be altered and the activation energy of diffusion changed.

Similarly the size of the initial clusters can potentially decrease due to the lower interface energy of the clean surface. However, the most important impact of a clean surface may be that clusters, have a preferred orientation with respect to the surface which has a profound effect during the grain growth/recrystallization phase.

It is also evident from Fig. S3 that a lowered substrate temperature improves the Pb film morphology. As described in section 1.1 the substrate temperature has an influence on almost all phases of the thin film growth evolution. Presumably the temperature in this case improves the film morphology by decreasing the density of initial clusters.

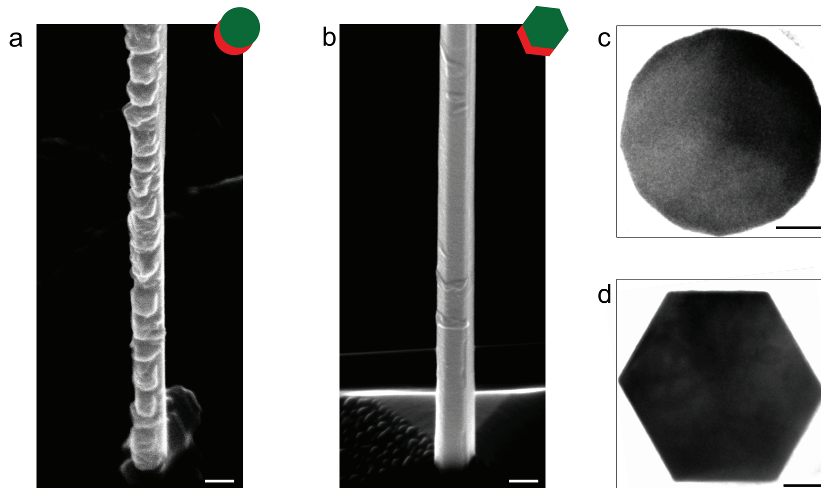

Figure S4: Impact of InAs nanowire faceting on Pb shell roughness. SEM micrographs of a round (**a**) and highly faceted (**b**) InAs nanowire. Scale bar is 200 nm in **a** and **b**. Bright field TEM micrographs of cross-sectioned round and highly faceted InAs nanowires are shown in **c-d**, respectively. Scale bar in **c** is 20 nm and 10 nm in **d**.

In Fig. S4 a round (**a**) and a highly faceted (**b**) InAs WZ nanowire are shown with 20 nm of Pb. The substrate temperature here is the same for both growths, $T_{sub} \sim 120$ K. From these SEM micrographs it is evident that Pb deposited on round nanowires forms a dewetted non-continuous film, whereas Pb deposited on highly faceted nanowires results in a smooth continuous film. Both films are deposited in-situ without breaking ultra-high vacuum in order to ensure chemically pure surfaces. The main difference between the two growths is the InAs/Pb interface energy. The interface of the faceted nanowire consist of high symmetry planes as calculated in section 3 whereas the round nanowire will have an interface energy related to all the micro-facets that make up the round nanowire. In the case where a low bi-crystal interfacial domain match is found, the interface energy is expected to be lower compared to a larger domain, promoting a more continuous film. Fig. S4 **c** and **d** show bright field TEM micrographs of a cross-sectioned round and highly faceted nanowire (the cross-sections are made using a microtome setup that involves water and therefore no Pb is observed, see section 5). Based on these experiments we can conclude that the interface energy plays a major role in the formation of thin and wetted films of Pb.

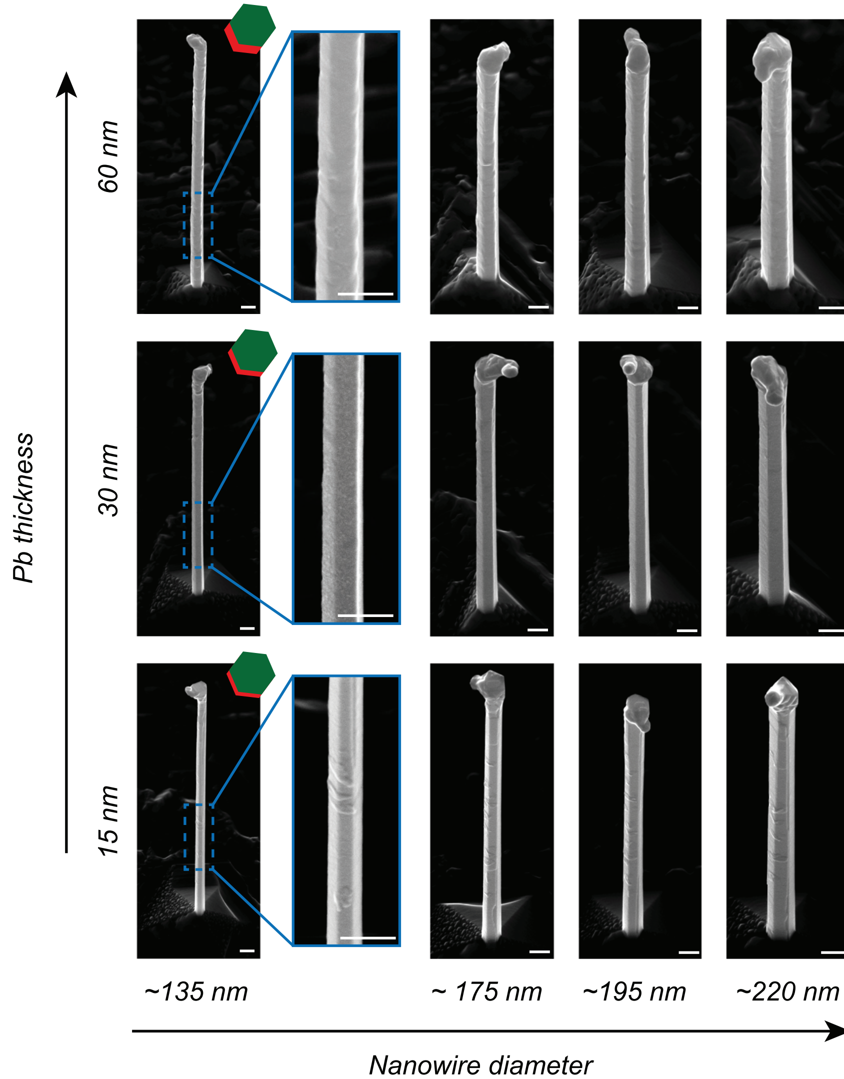

Figure S5: Overview of InAs nanowires with different dimensions for different Pb shell thicknesses. Scale bar for all micrographs is 200 nm.

In Fig. S5 continuous Pb shells were obtained for a wide range of nanowire diameters and Pb film thicknesses. Here three different thicknesses of Pb (15 nm, 30 nm, and 60 nm) were deposited on two facets of WZ InAs nanowires. In each growth the Au particle size catalyzing the nanowires was varied which yielded nanowires with a controlled, large range of diameters. We do not observe Pb film morphology dependence on nanowire diameter. This suggests that the incoherent grain boundary energy (see section 2) is not a major contributing factor to the thermodynamic driving force, as previously shown for Al on InAs in ref. [3]. The contribution to the overall excess energy from a grain boundary between adjacent facets scales with the film thickness whereas all other contributions also depend on the area of the facets [3]. This combined with the aforementioned rule of thumb that the grain boundary energy scales with the surface energy and the low surface energy of Pb (see

Table 2), indicates that the grain boundary energy is small in this configuration, presumably due to the wedge shaped inclusion which facilitates low energy grain boundaries (Fig. 1 (**e**) in main article).

In Fig. S5 we observe a tendency for the morphology to be more rough as the film thickness increases. We propose this to be related to a change in growth mode during the thin film growth. As discussed in the main article and section 1.1, the initial stages of thin film formation can be described via the island growth mode (Volmer-Weber). When the initial clusters impinge and perform grain-growth they will at some point, depending on the size and density of the initial clusters, form a continuous film. We propose that the subsequent growth of Pb films proceeds via layer-by-layer (Frank van der Merwe) growth. During the Pb deposition a constant large flux (~ 3 Å/s) was used to increase the density of initial clusters, see eq. 3. In the later stages the large flux increases the likelihood for new nucleation sites to be energetically favorable before the previous layer(s) is completed [1] and thus the thin film morphology may appear more rough. We expect that a varied flux during Pb deposition would result in a more uniform morphology but this was not pursued in order to keep the simplistic description of growth.

1.3 Controlling Al thin film growth

As previously described in Ref. [3], Al thin films on InAs nanowires were found in four different crystallographic orientations relative to the InAs facets $\{1\bar{1}00\}$. These are the $\{111\}$ and $\{11\bar{2}\}$ out of plane orientations with twins along the $\{111\}$ direction in both. The authors discuss that Al initially is in the low surface energy grain orientation (111) and then, due to incoherent grain-boundaries, changes to the $(11\bar{2})$ out of plane orientation when the Al film thickness increases. The authors similarly show how the $\{111\}$ out of plane orientation presents a flat morphology parallel to the nanowire facets whereas the $\{11\bar{2}\}$ grains have non-parallel surfaces. The change in thickness due to the presence of $\{11\bar{2}\}$ grains may have an influence on the hybrid device performance and thus a film only containing $\{111\}$ grains appears advantageous [16].

In Fig. S6 InAs nanowires with Al deposited on two facets using in-situ electron beam evaporation at $T_{\mathrm{sub}} \sim 120$ K are shown. Fig. S6 **a**,**b** show SEM micrographs of InAs nanowires with a 7 nm Al film deposited on an intentionally round nanowire. Here the film appears dewetted and discontinuous. In Fig. S6 **c**,**d** a 20 nm Al film is deposited on similar nanowires as in Fig. S6 **a** and **b**. The increased Al thickness seems to ensure a continuous film however with a rough morphology. Figure S6 **e** shows a selected area electron diffraction (SAED) pattern of a round InAs nanowire with a 20 nm Al film as in Fig. S6 **c**,**d** along the InAs $[11\bar{2}0]$ direction. Here the two different out of plane orientations ($[111]$,$[11\bar{2}]$) are observed and marked with red and blue circles, respectively. The light/dark blue and red indicate the respective twin variants. The four different grain orientations as previously found in Ref. [3] are thus confirmed.

In Fig. S6 **f**-**h** a 20 nm Al film is deposited on highly faceted InAs nanowires (as similarly shown for Pb in Fig. S4). Here the film morphology appears flat and continuous. Fig. S6 **i** shows a SAED pattern for a similar nanowire as shown in Fig. S6 **f**-**h** along the InAs $[11\bar{2}0]$ direction. Here only the $\{111\}$ out of plane orientation is observed and the change in nanowire morphology has thus reduced the number of Al grain orientation from 4 to 2.

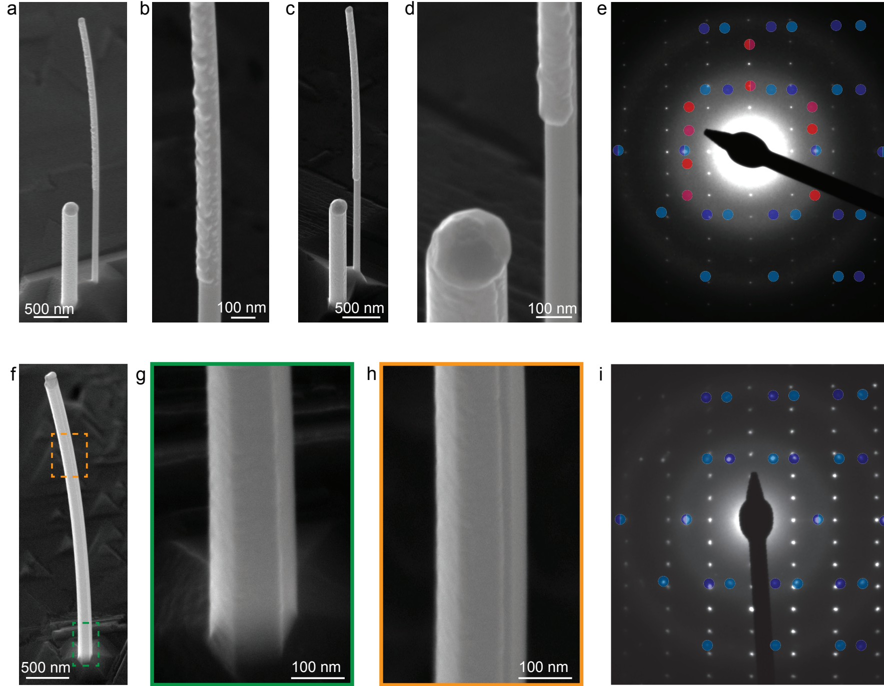

Figure S6: Al morphology on round and faceted nanowires. **a**,**b** dewetted and discontinuous 7 nm thick Al film on a round InAs nanowire. **c**, **d** continuous but rough 20 nm thick Al film on a round InAs nanowire. **e** SAED along InAs $[2\bar{1}\bar{1}0]$ direction of a nanowire similar to that in **c** and **d**, red and blue circles indicate the [111] and $[11\bar{2}]$ orientations respectively. **f-h** 20 nm thick Al film on highly faceted InAs nanowires. **i** SAED of a similar nanowire, only the [111] out of plane orientation is present, indicated by the blue circles.

The [111] out of plane orientation is preferred due to the out of plane surface being parallel to the nanowire facets as discussed previously. With this we showcase how the theoretical framework described in section 1.1 can be used to also optimize Al thin films.

2 Finding optimal single element materials for large-grain heteroepitaxial growth

In this section we focus on finding materials that allow for large-grain heteroepitaxial growth on nanowires with a thin and flat morphology. We propose a list of potentially interesting materials, based on the aforementioned considerations in section 1 and focus the search on single element materials with enhanced bulk superconducting properties relative to Al. We note that reports on hybrid devices utilizing disordered and polycrystalline superconducting films in some cases find essential material properties, such as hard-gap induced superconductivity, similarly to experiments using epitaxial films [17–19]. However, to take full advantages of the superconducting properties and to ensure as little disorder as possible we focus on

materials that can show large grain epitaxy. 12 elemental superconductors with key structural and physical parameters are shown in Table 1. To investigate which elements allow for a large grain heteroepitaxial growth on different semiconductor nanowires we start by addressing their ability to show grain growth/recrystallization. The kinetically limiting factors for grain growth via self-recrystalization or grain-boundary elimination/mobility are difficult to determine numerically in real systems. However, in all scenarios it depends on the cluster binding strength, or as a rule of thumb, the melting temperature of the nano-sized clusters. Because of this we disregard materials with a too high activation energy for grain boundary migration/recrystallization.

Table 1: List of single element superconducting materials. * Bulk (> 100nm films) values. X inferred for non-superconducting phase or missing critical field value, literature value for the grain boundary mobility activation energy and missing theoretical value for the average surface energy.

Element	Crystal structure	Lattice constant [Å]	$\bar{\gamma}$[20] [eV/Å^2]	T_m [C]	H [eV]	T_c^* [C]	H_c^* [T]
Nb	Cubic	3.3007[21]	0.134	2477	2.26[22]	9.09-9.465[21]	0.825[23]
Tc	Hexagonal	a = 2.735[21] c = 4.388[21]	0.163	2157	x	7.7-7.8[24, 25]	0.47[24]
Pb	Cubic	4.9502[21]	0.018	327	0.26[26]	7.175-7.23[21]	0.08[23]
V	Cubic	3.0282[21]	0.154	1910	2.17[27]	5.03-5.13[21, 28]	0.98[29]
α-La	Hexagonal	a = 3.770[21] c = 12.159[21]	0.046	919	x	4.8-5.0[21, 30]	x
Ta	Cubic	3.298[21]	0.146	3017	3.84[31]	4.39-4.482[21]	0.1[23]
β-Hg	Tetragonal	a = 3.995[21] c = 2.825[21]	0.004	-38.83	x	4.153[21]	0.04[23]
α-Sn	Cubic	6.4912[32]	0.034	232	0.43[33]	x	x
β-Sn	Tetragonal	a = 5.8314[21] c = 3.1814[21]	x	232	0.43[33]	3.701-3.722[21]	0.03[23]
In	Tetragonal	a = 4.5979[21] c = 4.9467[21]	0.019	156.6	0.17[34]	3.396-3.408[21]	0.275[23]
Re	Hexagonal	a = 2.760[21] c = 4.458	0.185	3186	x	1.699-2.42[21]	x
Tl	Hexagonal	a = 3.4566[21] c = 5.5248[21]	0.014	304	x	2.36-2.39[21]	0.017[23]
Al	Cubic	4.0496[21]	0.050	660	0.65[26]	1.171-1.196[21]	0.01[23]

Table 1 lists general structural parameters for 12 selected single element superconducting materials. From these we discard 7 due to either a too large activation energy for grain boundary migration or a too low melting temperature. We note that V, Nb, Ta deposited on nanowires have been shown, as expected, to form an amorphous/highly poly-crystalline film [2, 19], while Al and Pb is found to have a large grain heteroepitaxial match to nanowires [3, 18].

Table 2: List of single element superconducting materials. * Bulk (> 100nm films) values.

Element	T_C^* [K] [21]	H_C^* [T] [23]
Pb	7.2	0.080
Sn	3.7	0.030
In	3.4	0.275
Tl	2.4	0.017
Al	1.2	0.010

The 5 most likely single-element materials that would potentially be interesting for hybrid devices based on the aforementioned considerations are shown in Table 2. We discarded La in the list of candidates as we expect the substrate temperature needed to prevent a poly-crystalline films may be too high (especially for InAs nanowires). In the following we will analytically address the thermodynamic driving forces for each of the 5 elements. To estimate the interface energy we use basic geometry of high symmetry planes to find possible low interface domains and compare bulk values of the gamma surface space depth, i.e. how well defined the Wulff shapes are. In rough terms we expect that a material will experience strong thermodynamic driving forces if a discrete grain orientation has a low interface match with a low bulk residual mismatch and a low and discrete surface energy. In addition an incoherent grain boundary would potentially contribute more to the overall excess energy than a more coherent grain boundary. A more detailed procedure for finding the possible bi-crystal domain matches is found in Ref. [35].

To describe a certain bi-crystal interface we use the notation adopted from Ref. [3].

$$\left(\frac{N_{\parallel}^{SU}}{M_{\parallel}^{SE}}, \epsilon_{\parallel}\right) \times \left(\frac{N_{\perp}^{SU}}{M_{\perp}^{SE}}, \epsilon_{\perp}\right), \text{where } \epsilon = \frac{N_{SU} d_{SU}^{hkl} - M_{SE} d_{SE}^{hkl}}{M_{SE} d_{SE}^{hkl}} \times 100. \tag{4}$$

Here SU and SE indicate the superconductor and semiconductor parallel ($\parallel$) or transverse ($\perp$) to the growth direction and ϵ denotes the bulk residual mismatch between N superconducting planes and M semiconducting planes.

2.1 Aluminium

Al has already been proven as an especially interesting material for superconducting experiments with InAs, InAsSb and InSb nanowires [3, 36, 37]. Al has the unique material characteristic that it forms a self-terminating oxide layer which makes it optimal for post-growth device processing and reliable tunnel-junctions. This also makes Al very resistant towards dewetting.

If Al is deposited on a relatively low surface energy material such as InAs facets, it is found to form large grains, as discussed in section 1.3. If growth parameters such as substrate temperature are optimized a thin and continuous film can be easily obtained. Al has the highest activation energy for grain boundary migration of the selected materials and is always found with a face centered cubic (FCC) crystal structure. The Wulff shape structure reveals very deep cusps in the gamma surface space around (111) and (100) planes [20]. As already discussed in section 1.3 Al deposited on InAs nanowires is found with either [111] or [11$\bar{2}$]

out of plane orientations where both of these form twin planes along the [111] direction effectively yielding 4 different orientations of Al on InAs. The lowest bi-crystal interfaces are found to be

$$\left(\frac{3_{[11\bar{2}]^*}}{1_{[0001]}}, 5.9\%\right) \times \left(\frac{3_{[1\bar{1}0]}}{4_{[11\bar{2}0]}}, 0.49\%\right) \text{ and } \left(\frac{3_{[111]}}{1_{[0001]}}, -0.15\%\right) \times \left(\frac{3_{[1\bar{1}0]}}{4_{[11\bar{2}0]}}, 0.49\%\right) \quad (5)$$

where $*$ denotes corrected interface planes such that only Al atoms at the InAs surface are used in the calculations. We note that these values are given as bulk calculations with the parameters stated in Table 3 which generally give a discrepancy to Ref. [3], where the planes are given as interfacial planes. Considering the above, Al has strong thermodynamic driving forces towards discrete orientations on InAs nanowires, however, the large activation energy for grain boundary migration causes smaller grains. This corresponds well with the experimental observations.

2.2 Thallium

Tl is commonly found with a hexagonal close-packed (HCP) crystal structure with average surface energy comparable to Pb and deep cusps in the gamma surface space around $\{0001\}$, $\{1\bar{1}00\}$ and $\{11\bar{2}0\}$. For this material the best bi-crystal interfacial match was found to be

$$\left(\frac{4_{[11\bar{2}0]}}{1_{[0001]}}, -1.6\%\right) \times \left(\frac{4_{[1\bar{1}00]}}{3_{[11\bar{2}0]}}, 5\%\right) \quad (6)$$

The melting temperature of Tl is very close to Pb which combined with the interestingly low interfacial domains and bulk residual mismatch make Tl structurally a very promising material. We expect Tl deposited with similar growth parameters as for Pb to yield a large grain heteroepitaxial match to InAs facets. Based on the interface mismatch calculation above we expect more than one out of plane orientation to be energetically favorable causing axial grain boundaries. We note that Tl is highly toxic and has radioactive isotopes.

2.3 Indium

In is found theoretically to have two different crystal structures - tetragonal body-centered (TBC) and hexagonal. Both of these have deep cusps in the surface gamma space with low surface energies. However, as no experimental reports on free In with hexagonal crystal structure were found we focus on TBC structure. Indium in TBC has deep cusps around the [101] direction in the gamma plot and thus we believe that this will be the out of plane orientation. The best theoretical bi-crystal interfacial matches are depicted in Table 3, and the most probable was found to be

$$\left(\frac{3_{[100]}}{2_{[0001]}}, -1.8\%\right) \times \left(\frac{1_{[010]}}{2_{[11\bar{2}0]}}, 7.6\%\right) \quad (7)$$

In on WZ InAs nanowire facets appears to have a good match in the axial direction whereas in the transverse the domain is small but the bulk residual mismatch is large. In addition, In has the lowest melting temperature of all the selected materials, and is

therefore vulnerable to dewetting. Under the assumption that the melting temperature is tied to the activation energy for diffusion (as discussed in section 1) the low melting point may lead to a larger diffusion constant. This may again cause a lower density of stable clusters thus a relatively larger distance between the initial clusters. Compared to Pb, In has a similar average surface energy, however, the low melting point indicates a low binding energy. Because of this we would expect the initial In clusters to be larger than Pb. As Pb also appears to be vulnerable to dewetting if the growth parameters are not optimized, we suggest that In will form large dewetted islands on an InAs nanowire if optimized in a similar way.

We propose that In under the right growth optimization (very low substrate temperature < 120K and high flux) may form large grain heteroepitaxial match to InAs facets for relatively thick films (> 20nm). In addition a short flux of Sb before the In deposition may improve the wetting probability. This is due to the surfactant effect of Sb, where Sb atoms on the surface influence the surface energy reducing the adatom average displacement [38].

2.4 Tin

Sn is theoretically found to have two very different crystal phases, namely cubic and tetragonal (α, β), see Table 3. Depending on the crystal structure Sn can be a semi-metal (α phase) or a superconductor (β phase) [18]. In this article we are mainly interested in materials that have superconducting properties and therefore focus on the β phase. The grain boundary mobility for Sn is found from literature to be similar to Pb, see table 2. The melting point, is lower compared to Pb whereas the mean surface energy is larger. From this we would expect a thin film of Sn to be vulnerable to dewetting. Sn has a complicated Wulff shape structure with no discrete well defined cusps. This will have significant influence on the grain growth evolution as no distinct out of plane or in-plane orientation dictates a specific grain orientation relative to the nanowire facet. We therefore expect a thin Sn film to be poly-crystalline with grain size mainly dependent on the substrate temperature. As seen in table 1, Sn may find some specific orientations that would minimize the interface energy, however, the low temperature needed to prevent dewetting would also limit the grain growth needed for impinging cluster recrystallization. These considerations are consistent with the experimental investigation in Ref. [18]. We emphasize that Sn deposited on InAs without the surfactant Sb is likely to yield a dewetted film.

Table 3: List of probable InAs - superconductor bi-crystal interfaces

Element	hkl	Axial domain size ([0001])	Residual mismatch [%]	Transverse domain size ([11$\bar{2}$0])	Residual mismatch [%]
Pb	001	3:2	5.70	3:7	-0.73
Pb	11$\bar{2}$*	5:2	7.88	2:3	-5.44
Pb	110	2:1	-0.35	3:5	-1.73
Pb	111	5:2	1.71	3:4	0.30
Al	001	5:3	-3.92	1:2	-5.25
Al	11$\bar{2}$*	3:1	5.90	6:7	-0.54
Al	110	5:2	1.90	3:4	0.49
Al	111	3:1	-0.15	1:1	9.40
In	001	3:2	5.62	3:7	-0.80
In	100	3:2	-1.82	1:2	7.57
In	110	2:1	-7.44	2:3	1.42
In	011	2:1	-4.12	2:3	5.06
In	111	5:2	-3.31	4:5	1.70
β-Sn	001	2:1	-9.43	2:3	-0.76
β-Sn	011	5:2	-0.61	3:4	-1.99
β-Sn	100	6:5	-0.39	1:3	-9.04
β-Sn	110	5:3	-2.17	1:2	-3.53
β-Sn	111	3:1	7.57	6:7	1.02
α-Sn	100	1:1	-7.60	1:3	1.25
α-Sn	110	3:2	-1.99	1:2	7.39
α-Sn	111	2:1	6.70	4:7	0.21
α-Sn	11$\bar{2}$*	7:4	-0.98	1:2	-7.00
Tl	0001	5:4	-1.69	1:2	4.30
Tl	11$\bar{2}$0	4:1	-1.59	5:4	1.09
Tl	1$\bar{1}$00	5:2	6.53	3:4	5.05

3 Pb epitaxy

In this section we present a more in-depth investigation of the InAs/Pb structural relation and highlight the key material properties that led us to choose Pb. Thin films of Pb are always found with an FCC crystal structure and a low average surface energy with pronounced cusps in the gamma surface space around (111) with an area fraction of more than 0.5 [20]. Pb on InAs is theoretically found to have a particularly well ordered large grain heteroepitaxial match as discussed in the main article. This is most prominent along the axial direction where each (0001) plane of InAs corresponds to two {1$\bar{1}$0} planes in Pb. The fact that an interfacial domain with (1$\bar{1}$0) planes is similar to a domain with ($\bar{1}$10) planes theoretically allows for grain boundaries along the transverse direction ([11$\bar{2}$0]/[11$\bar{2}$]). The low activation energy for grain boundary mobility and strong thermodynamic driving

force for a single crystal, however, suggest that very few grain boundaries in Pb should be energetically possible.

3.1 InAs/Pb epitaxy

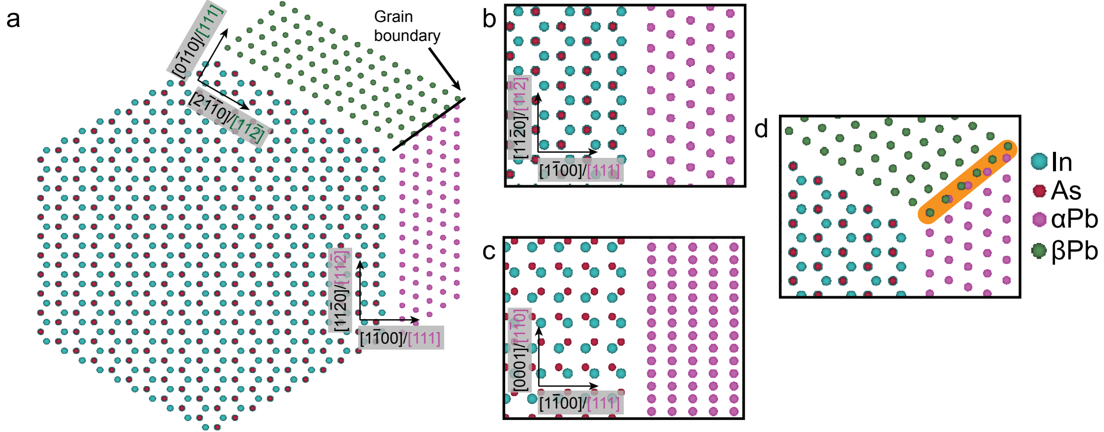

Figure S7: Simulations of InAs/Pb heterostructure [39]. **a** Model of WZ InAs/Pb heterostructure viewed along the $[0001]/\{1\bar{1}0\}$ direction. The theoretically suggested incoherent grain boundary between the two single Pb crystals on adjacent facets is marked by the black line. **b** Close-up on the interface between InAs and Pb along the transverse direction ($[0001]/[1\bar{1}0]$). **c** InAs and Pb interface viewed parallel to the nanowire facet ($[11\bar{2}0]/[11\bar{2}]$). **d** Close-up on the corner of the nanowire where Pb theoretically may form an incoherent grain boundary highlighted by the orange bar.

In Fig. S7 **a** a simulation of Pb on two facets of an InAs nanowire is shown similar to the simulations in Fig. 1 in the main article. Here Pb atoms on the two adjacent facets are colored differently for clarity. To estimate the relative orientations of Pb to the nanowire facet we assumed the out of plane orientation to be the lowest surface energy (111) plane. Subsequently the best bi-crystal interfacial match was found as described above and depicted in Table 3. From this we get an extraordinarily low bi-crystal domain match with a low bulk residual mismatch along the axial direction, see Fig. S7 **c**. Here two $\{1\bar{1}0\}$ planes of Pb correspond to each [0001] plane of InAs. On the transverse direction, however, two possible matches were found and the collective interface can be described as

$$\left(\frac{2_{[1\bar{1}0]}}{1_{[0001]}}, -0.3\%\right) \times \left(\frac{2_{[11\bar{2}]^*}}{3_{[11\bar{2}0]}}, -5.4\%\right) \tag{8}$$

and

$$\left(\frac{2_{[1\bar{1}0]}}{1_{[0001]}}, -0.3\%\right) \times \left(\frac{3_{[11\bar{2}]^*}}{4_{[11\bar{2}0]}}, 6.4\%\right). \tag{9}$$

In Fig. S7 **d** a high energy incoherent grain boundary is formed on the nanowire corner when the two single crystal Pb grains (pink, and green phase) merge. The unknown position of the grain boundary atoms are marked with an orange bar. From high angle annular dark

field scanning transmission electron microscope (HAADF STEM) investigations it is observed that instead of forming an incoherent grain boundary as suggested by the simulations in Fig. S7 a wedge-shaped single-crystalline domain is formed (see Fig. 1 in main text). The wedge-shaped grain allows the formation of two coherent grain boundaries, thereby reducing the grain boundary energy between the single Pb crystals.

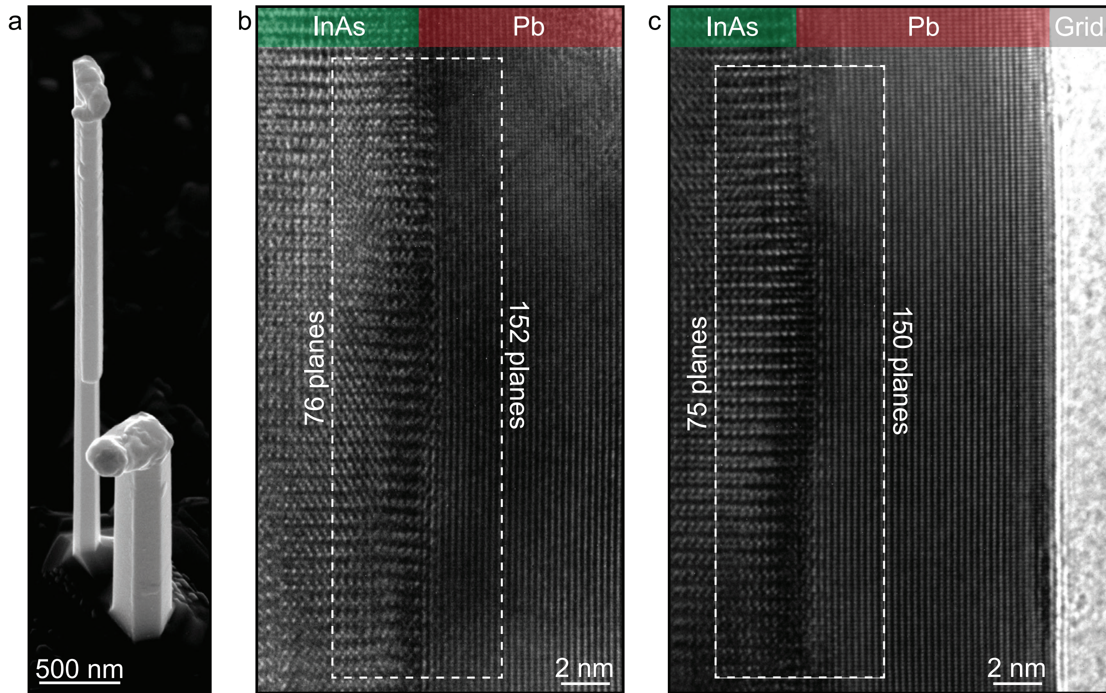

Figure S8: Pb match to InAs in the axial direction. **a** SEM micrograph of a shadowed InAs nanowire covered with 20 nm of Pb on two nanowire facets. **b-c** HR-TEM micrographs of InAs/Pb nanowire hybrids. Here the nanowire is viewed along the facet ([11$\bar{2}$0]). Burgers circuits are used to determine the lattice match between the two materials and in both cases a 2:1 match between Pb and InAs is found without any dislocations.

In Fig. S8 a 20 nm film of Pb is deposited in-situ on highly faceted InAs nanowires on two facets. Fig. S8 **a** shows an SEM micrograph of two nanowires. The thicker nanowire in front is used to produce a shadow in the Pb film on the wire behind it. This procedure is similarly used to produce the shadows in the Pb film as seen in main article (Fig. 2). From the SEM micrograph a continuous and morphologically flat film of Pb is observed. Near the top of the nanowire the Pb appears more rough which is likely due to an increased amount of stacking faults. As described in the methods section of the main article, the procedure used to produce the highly faceted nanowires includes a lower temperature growth step. This commonly generates more stacking faults near the top of the nanowire. In Fig. S8 **b** and **c** two HR-TEM micrographs of the bi-crystal interfacial matches between InAs and Pb from two different nanowires are shown. On top of the micrographs Burgers circuits are used to

count the amount of planes in InAs and Pb. This enables a comparison of the theoretical and the experimentally observed axial match. From this we find no dislocations and propose that the bulk residual strain may be relaxed by straining InAs and/or Pb.

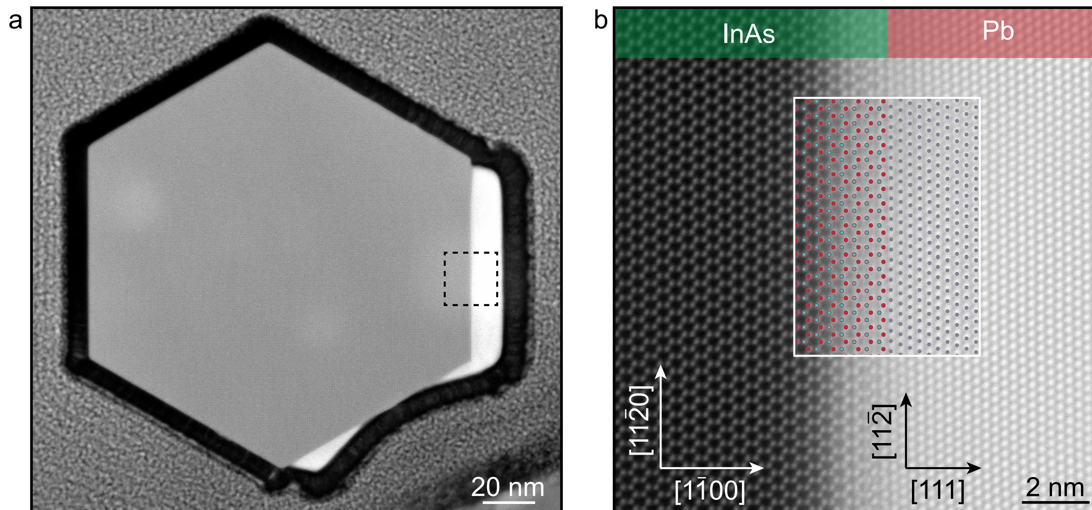

Figure S9: Pb match to InAs in the transverse direction. **a** HR-HAADF-STEM micrograph of a cross-sectioned InAs (gray) nanowire with Pb (white) on two facets covered by a full shell of Si (black). Bi-crystal interface between InAs and Pb overlaid with a simulated relaxed match is shown in **b**.

Fig. S9 shows HAADF STEM micrographs of a cross-sectioned highly faceted InAs nanowire with 20 nm of Pb deposited on two facets and covered by a 10 nm full shell of Si. The cross-section specimen was made using a focused ion beam - scanning electron microscope (FIB-SEM) where additional Pt was deposited to protect the InAs/Pb during the FIB process [40]. The Pb film in this cross-section was partly shadowed which prevented an analysis of the grain boundary between Pb on adjacent facets (see Fig. S7 **c**). However the cross-section from a different nanowire presented in the main article showed how a wedge-shaped single crystal accommodates two low energy grain boundaries. In Fig. S9 **b** a HR-HAADF-STEM micrograph together with the simulated relaxed bi-crystal interfacial match from Fig. S7 **b** along the [11$\bar{2}$0]/[11$\bar{2}$] direction is shown. The simulation is placed such that it fits the WZ InAs nanowire and the Pb near the top of the white box. Comparing the micrograph to the simulation it can be seen that the observed structure is not relaxed as the Pb atoms in the micrograph deviate from the simulation towards the bottom of the white box.

Utilizing the [1$\bar{1}$00] plane distance as a local scale, Pb along the [11$\bar{2}$] direction was measured to be compressively strained ~ 1.7 % whereas InAs along [11$\bar{2}$0] direction was found to be tensile strained ~ 0.7 %.

Assuming that the [1$\bar{1}$00] planes are not heavily influenced by the strain caused by the interface the compressed Pb and expanded InAs planes indicate that the bi-crystal interfacial match is best described by eq. 9, despite that the interface with a 3:4 match (eq. 8) has a

theoretically smaller interfacial domain and a smaller bulk residual mismatch. One possible explanation for this, is that the planes with dangling bonds (surface atoms) mainly contribute to the minimization of the interface energy. By only considering surface atoms the bi-crystal interface is described as

$$\Big(\frac{2_{[1\bar{1}0]}}{1_{[0001]}}, -0.3\%\Big) \times \Big(\frac{3_{[11\bar{2}]^*}}{2_{[11\bar{2}0]}}, 6.4\%\Big). \tag{10}$$

Even though a perfect epitaxial match is not fulfilled in the transverse direction we expect that the two possible matches (3:2 and 4:3) combined allow for a low surface energy.

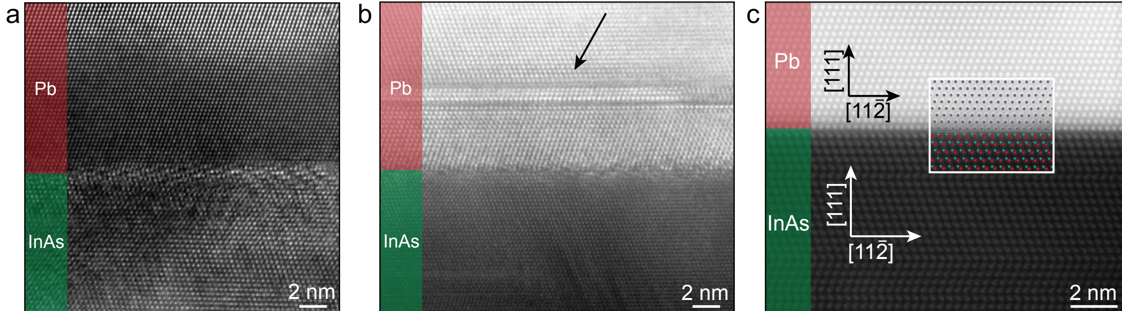

Figure S10: Pb match to InAs “kink”. **a** HR-TEM micrograph of InAs “kink” covered with Pb. **b** HR-TEM micrograph of InAs “kink” covered with Pb where a twin in Pb can be observed. **c** HR-HAADF-STEM micrograph of the bi-crystal interface between InAs “kink” and Pb overlaid with a simulated relaxed match.

To compare the InAs/Pb bi-crystal interfacial match with another crystallographic orientation and morphology of the InAs nanowire, a 20 nm film of Pb was deposited on a “kinked” nanowire. Here the nanowire growth direction was changed from [0001] to the $\{1\bar{1}00\}$ direction as similarly shown in Ref.[41]. The change in growth direction also induces a different nanowire morphology where the kinked part of the nanowire has a square morphology with a [0001] facet at the top. Another consequence of the changed growth direction is that the InAs overgrowth now has the possibility to grow with a ZB crystal structure. This can be seen in Fig. S10 **a** - **c**. In Fig. S10 **b** low energy grain boundaries along the [111] direction is observed as opposed to the single crystal nature when deposit on $\{1\bar{1}00\}$ facets. In Fig. S10 **c** a relaxed simulation of the expected match is placed on top of the micrograph. Here no strain is observed and we expect both InAs and Pb to be relaxed. The expected best bi-crystal domain match between InAs and Pb on a kink was found to be

$$\Big(\frac{4_{[11\bar{2}]^*}}{5_{[11\bar{2}]}} - 2.0\%\Big) \times \Big(\frac{5_{[1\bar{1}0]}}{4_{[1\bar{1}0]}} 2.1\%\Big) \tag{11}$$

3.2 Other semiconductors/Pb

In the previous section we demonstrated how Pb is capable of forming exceptionally well ordered large grains epitaxially matched to InAs nanowires. By using the procedure outlined

in section 2 we have calculated residual mismatch and domain size for other III-V materials that would potentially form an epitaxial match with Pb. The results for GaAs/Pb and InSb/Pb hybrids are shown in table 4. We note that optimized depositions of Pb on substrates containing trace amount of Sb (like InAsSb or InSb) will likely show a similar wetted morphology as when deposited on InAs. This is primarily due to the surfactant effect of Sb that effectively have been found to relax the interface and thereby lowering the interface energy [42].

Table 4: List of probable GaAs - Pb and InSb - Pb bi-crystal interfaces

III-V	hkl of Pb	Axial domain size ([111])	Residual mismatch [%]	Transverse domain size	Residual mismatch [%]
GaAs	001	2:3	1.11	4:5 ([110])	-0.93
GaAs	110	1:1	7.24	8:7 ([110])	0.07
GaAs	111	8:7	0.07	7:5 ([110])	0.09
GaAs	$11\bar{2}$	1:1	-7.12	4:3 ([110])	1.11
InSb	001	3:4	-0.72	1:2 ([$11\bar{2}$])	-6.40
InSb	110	1:1	-6.40	3:4 ([$11\bar{2}$])	-0.72
InSb	111	4:3	1.90	1:1 ([$11\bar{2}$])	8.08
InSb	$11\bar{2}$	5:4	1.33	7:8 ([$11\bar{2}$])	0.31

4 Additional transport data

4.1 Spectroscopy on half-shell InAs/Pb nanowires.

Here we investigate the gate dependence of the superconducting gap using the tunnel junction device shown in Fig. S11 **a**, and Fig. 3 in the main-text. After the tunnel junction (indicated by the white arrow) is established by tuning the voltage of the two side gates, V_G, we record the differential conductance, g, as a function of the source/drain bias, V_{SD}, and the back-gate voltage, V_{BG}. The result of this measurement is shown in Fig. S11 **b**, in which we observe a strongly suppressed g for $|V_{SD}| < 1.2$ mV, corresponding to a superconducting energy gap of $\Delta \sim 1.2$ meV [43]. The intensity modulations outside the gap likely arise from impurity-related quantum dots in the tunnel barrier [44]. We emphasize that the observed Δ is independent of V_{BG} across a range of 5 V, and independent of the above gap resonances, ruling out Coulomb charging effects as the origin of the suppressed conductance.

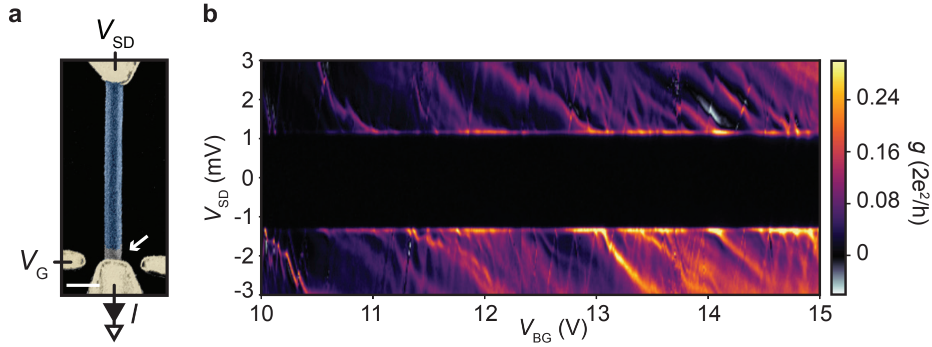

Figure S11: **Additional data on tunnel spectroscopy on an InAs/Pb nanowire. a,** False-coloured SEM micrograph of the measured InAs/Pb tunnel junction device. Yellow, Ti/Au contacts; Blue, Pb. Scale-bar is 200 nm. **b,** Differential conductance as a function of V_{SD} and V_{BG} showing a hard induced superconducting gap with constant gap size of $\Delta \sim$ 1.2 meV over a gate range of 5 V.

4.2 Coulomb spectroscopy on InAs/Pb islands

In this section we compare the Coulomb blockade behavior of the InAs/Pb island device presented in the main text in parallel and perpendicular magnetic field directions. First, we show Coloumb blockade spectroscopy data recorded in perpendicular magnetic fields. Next, we present a peak-shift analysis of zero-bias Coulomb resonances evolved in parallel magnetic fields (raw data presented in Fig. 4, main-text), and finally we compare the peak-shift of the two directions.

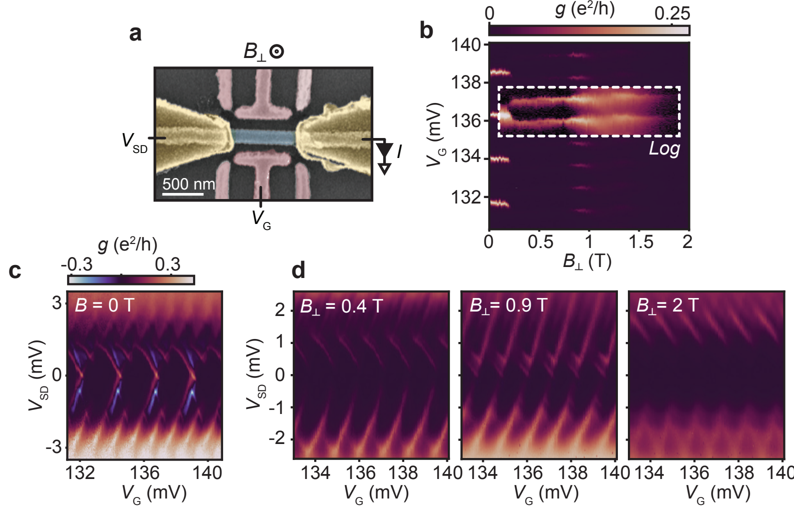

Figure S12: **InAs/Pb Coulomb island in perpendicular magnetic fields. a,** False-colored SEM micrograph of an InAs/Pb island device. Yellow and pink, Ti/Au contacts and gates, respectively; Blue, Pb. Perpendicular magnetic field direction is indicated by $B_\perp$. **b,** Conductance as a function of V_G and $B_\perp$ showing evenly spaced Coulomb resonances that split abruptly at $B_\perp \sim 0.2$ T. Inset shows the same data on a logarithmic scale to highlight the split. **c,** Differential conductance at zero field as a function of V_G and V_SD showing evenly $2e$-spaced Coulomb diamonds with asymmetric lead coupling. **d,** Same Coulomb diamonds shown in (**c**) recorded at $B_\perp = 0.4$, 0.9 and 2 T.

4.2.1 InAs/Pb island in perpendicular magnetic fields

Figure S12 **a** shows an SEM image of the InAs/Pb island device presented in Fig. 4 in the main text, where source/drain bias, gate voltage and the perpendicular magnetic field direction are indicated by V_SD, V_G and $B_\perp$, respectively. In Fig. S12 **b** we show the differential conductance, g, at zero-bias measured as a function of V_G and $B_\perp$. Here evenly spaced Coulomb peaks are evident up to $B_\perp \sim 250$ mT, after which they abruptly split, with decreased intensity. The dashed white box shows the same data plotted on a logarithmic scale for clarity. The constant spacing between Coulomb resonances for $B_\perp > 250$ mT will be discussed in section 4.2.2.

Figure S12 **c** corresponds to the data in Fig. S12 **b** and shows g, as a function of V_SD and V_G at $B = 0$ T. This stability diagram shows evenly spaced Coulomb diamonds with

a pronounced difference in g at high bias, which may be due to an asymmetry in the lead couplings. At the onset of each Coulomb diamond, regions with negative g appear which are due to transport blockade by single-electron/hole excitations. At low bias, Coulomb diamonds appear periodically in gate voltage with a spacing of ~ 2 mV, whereas for $|V_{SD}| > 1.2$ mV periodic features are observed with half this gate voltage spacing. This suggests that the charge of the island for $|V_{\mathrm{SD}}| < 1.2$ mV is quantised in units of $2e$ due to the superconducting state, whereas for $|V_{\mathrm{SD}}| > 1.2$ mV single-electron charging occurs as $|V_{\mathrm{SD}}| > \Delta/e$. In Fig. S12 **d** we show stability diagrams in a similar gate and bias voltage region, recorded at perpendicular magnetic fields of $B_{\perp} = 0.4$, 0.9 and 2 T. We observe a decrease in g at low bias with respect to zero magnetic field, which may be due to field dependent lead couplings or interactions with device-specific quantum dots formed in the nanowire.

4.2.2 Analysis of the Coulomb-peak spacings

Previous studies on hybrid nanowire devices have focused on the magnetic field dependence of the Coulomb-peak spacings in the context of hybridized Majorana modes at the ends of the nanowire [45]. Oscillations in the peak spacings are expected to be a signature of the hybridization and are exponentially suppressed as the distance between the Majorana modes is increased. For comparison with aluminum-based hybrid nanowire devices we discuss here the magnetic field evolution of the Coulomb-peak spacings of the InAs/Pb island. We focus on the Coulomb-blockade spectroscopy measurements shown in Fig. 4**b** of the main text.

In order to accurately determine the peak positions we fit each gate-voltage trace with a function containing multiple Gaussian functions on top of a constant background. To limit the number of fitting parameters we restricted the analysis to the gate voltage range: $V_{\mathrm{G}} = 440$ mV to $V_{\mathrm{G}} = 449$ mV, in which 8 peaks can be clearly identified at high magnetic field. The strong asymmetry in intensity between the two sets of Coulomb peaks at low magnetic fields limits our analysis to the range $B_{\parallel} > 0.8$ T for which 8 peaks could be reliably fitted (see Fig. S13**b**). Figure S13**a** marks the center positions of the Coulomb peaks obtained from the fit by blue circles. For completeness we show the peak-center positions also in the range $B_{\parallel} < 0.8$ T for which we reduced the number of Gaussian functions to 4 to ensure reliable fit results. We distinguish between the peak spacings in the even charge states and the odd charge states as indicated by S_{e} and S_{o}, respectively. The full width at half maximum (FWHM) of the Coulomb peaks was ~ 0.3 mV at zero magnetic field and 0.6 mV at $B_{\parallel} = 2.3$ T.

The average values of the peak spacings for $B_{\parallel} > 0.8$ T are shown in Fig. S13 **c**. Near $B_{\parallel} = 0.8$ T the difference between $S_{\mathrm{e,avg}} \approx 1.3$ mV and $S_{\mathrm{o,avg}} \approx 0.8$ mV implies that the island is well within the even-odd regime at this magnetic field. Around $B_{\parallel} = 1.5$ T the even- and odd spacings become equal and a regular 1e-spaced Coulomb-peak pattern is obtained. At even higher fields $S_{\mathrm{e,avg}}$ and $S_{\mathrm{o,avg}}$ appear to converge to different values. This might be the onset of an oscillation as observed in [45] although we could not confirm this due to the instability of the device at higher magnetic fields. The modulation of the peak spacing in the fitted range does suggest that the doubling of the Coulomb peaks is not due to quasiparticle poisoning or the quenching of superconductivity for which a uniform 1e spacing is expected [46].

We performed the same Coulomb-peak analysis in a different gate-voltage range of the

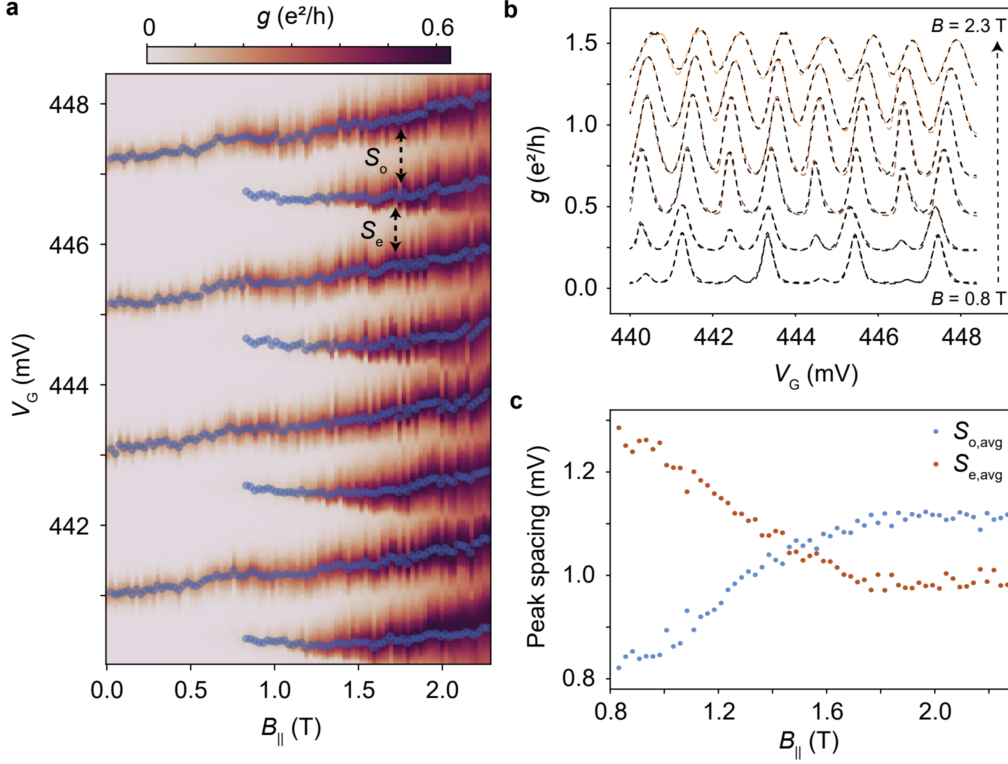

Figure S13: **Magnetic-field evolution of the Coulomb-peak spacings.** **a,** Fitted Coulomb-peak center positions (blue circles) in the Coulomb-blockade spectroscopy data of Figure 4**c** (main text) in the gate-voltage range $V_G = 440$ mV to $V_G = 449$ mV. **b,** Selection of gate-voltage traces from **a** with the fitted traces superimposed (dashed lines). **c,** Magnetic-field dependence of the average even- and odd Coulomb-peak spacings.

same device for both the parallel magnetic field $B_{\parallel}$ as well as the perpendicular magnetic field $B_{\perp}$. The results are presented in Fig. S14. For the parallel magnetic field we again observe a strong modulation of $S_{e,avg}$ and $S_{o,avg}$ where in this case we are able to resolve a complete oscillation. In contrast, the same measurement in the perpendicular magnetic-field direction shows no measurable oscillations. The uniform 1e-spacing may suggest that superconductivity was quenched around $B_{\perp} = 0.2$ T, or may be a result of one or more trivial bound states converging around zero energy [47–49].

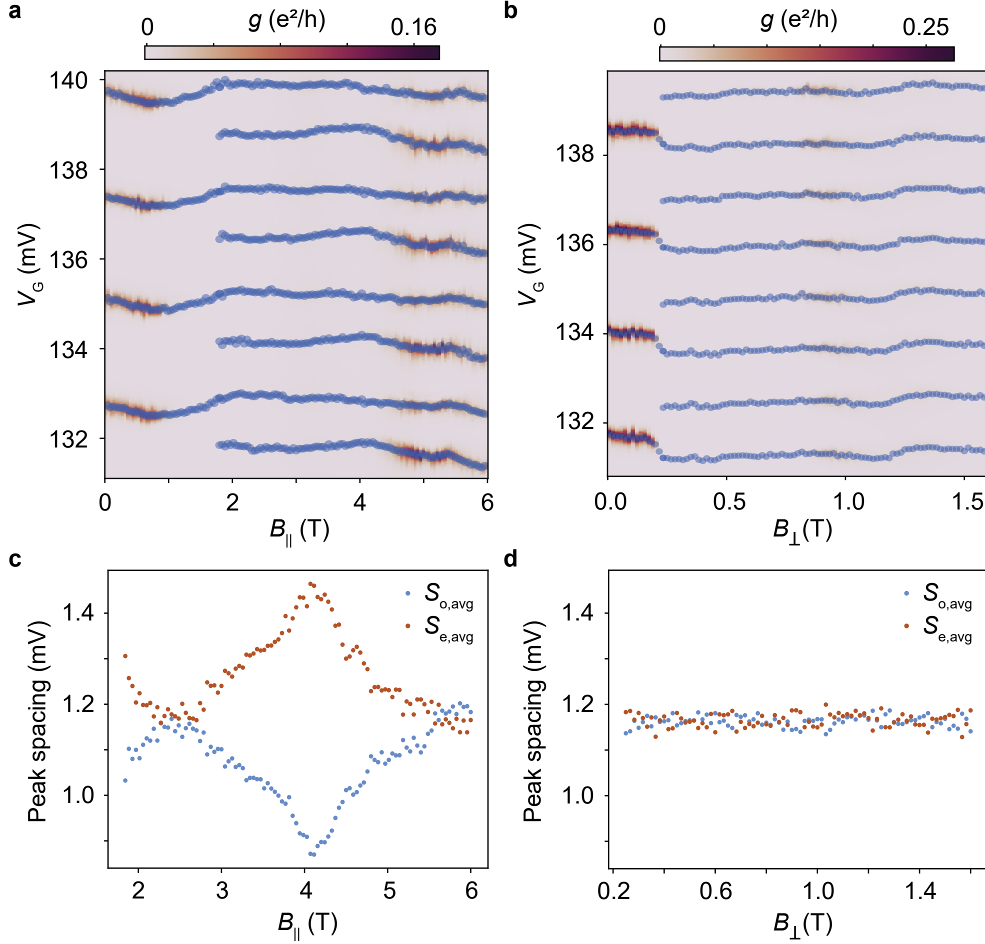

Figure S14: **Coulomb-peak spacing evolution in a different gate-voltage range. a,** (**b**) Fitted Coulomb-peak center positions for parallel (perpendicular) magnetic field. **c,** (**d**) Magnetic-field dependence of $S_{\mathrm{e,avg}}$ and $S_{\mathrm{o,avg}}$ for parallel (perpendicular) magnetic field.

4.3 Tunnel spectroscopy on full-shell InAs/Pb nanowires

In this section we present preliminary tunnel spectroscopy measurements of 'full shell' nanowires, with Pb grown on all six InAs facets [50]. We show an SEM micrograph of a full shell nanowire in Fig. S15 **a** with the inset showing a schematic cross-section of the nanowire (green, InAs; blue, Pb). Tunnel spectroscopy devices based on full shell InAs/Pb nanowires were fabricated in a similar way to those presented in Fig. 3 (main text) and Fig. S11, as seen in the micrograph in Fig. S15 **b**.

The red trace in Fig. S15 **c** shows differential conductance, g, as function of source drain bias, V_{SD}, where g is suppressed below the coherence peaks at $V_{\mathrm{SD}} \sim \pm 0.8$ mV. The extended dependence on back-gate voltage, V_{BG}, presented in Fig. S15 **d**, shows that this corresponds to the superconducting gap value of $\Delta \sim 0.8$ meV, across the entire 150 V V_{BG} range. It is not clear whether the smaller Δ compared to half-shell devices (Figs 3,4 of the main text) is a systematic effect of the full-shell geometry, or is an isolated feature of this particular device. The discrete V_{BG}-dependent states arising for $|V_{\mathrm{SD}}| < \Delta/e$ are confinement-related bound

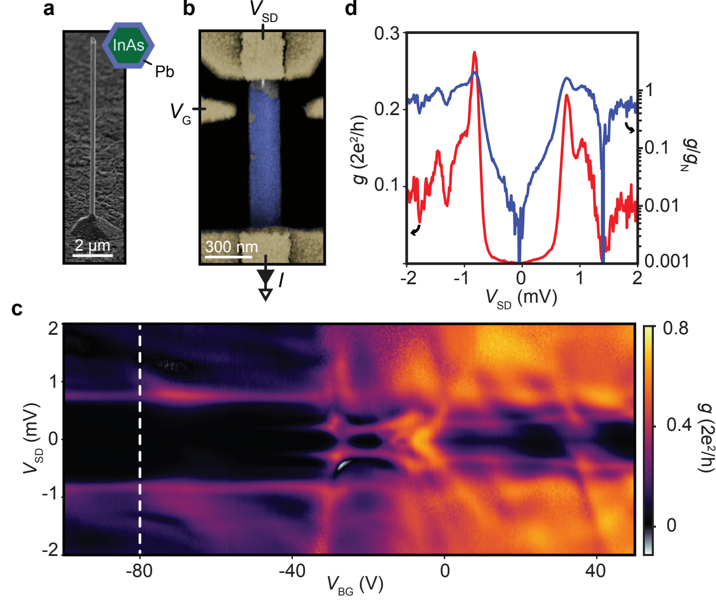

Figure S15: **Tunnel spectroscopy on full-shell InAs/Pb nanowires. a,** SEM micrograph of an InAs nanowire with Pb grown on all six facets. Schematic represents cross-section of the nanowire (green, InAs; blue, Pb). **b,** False-coloured SEM micrograph of the InAs/Pb tunnel junction device, with the tunnel junction (gray) located between the top gold (yellow) contact and the Pb shell. **c,** Differential conductance recorded as a function of V_{SD} and backgate voltage, V_{BG} showing a superconducting gap with a size of $\Delta \sim 0.8$ meV. Gate-dependent sub-gap states are visible between V_{BG} = -40 V to 50 V. **d,** Differential conductance (left axis, red trace) as a function of source-drain bias showing strongly suppressed conductance at low bias. Right axis (blue trace) shows the normalized differential conductance on a logarithmic scale, indicating a conductance suppression of two orders of magnitude around $V_{\mathrm{SD}} = 0$.

states arising from the semiconductor/superconductor coupling. These may be Yu-Shiba-Rusinov bound states, in the case where a quantum dot forms in the bare InAs segment, and the spin on the quantum dot couples to the superconductor [44, 51]. They may also be Andreev bound states arising as hybrid nanowire states in the semiconductor/superconductor (Pb/InAs) segment, in a superconducting analogue to particle-in-a-box states [52, 53].

We plot g normalized to the normal state conductance, $g_{\mathrm{N}} = g|_{V_{\mathrm{SD}}=2\mathrm{mV}}$, on the right axis of Fig. S15d, which shows that conductance is suppressed by over two orders of magnitude around $V_{\mathrm{SD}} = 0$, consistent with the hard gap observed in half shell devices. However, g increases steadily as V_{SD} approaches $\pm\Delta/e$, producing an overall ‘U’ or ‘V’ profile, indicating the presence of non-negligible sub-gap conductance. There are several possible causes for this behaviour. For our device, the low coupling of V_{BG} to the InAs segment makes it difficult to fully deplete the tunnel junction within a gate range that would avoid dielectric breakdown (±100 V). Increasing transmission through the tunnel barrier can give rise to a non-ideal gap profile, as explored in Zhang *et al.*[54]. Alternatively, the profile may be due to a high density of discrete Yu-Shiba-Rusinov and/or Andreev bound states arising from

quantum confinement effects in the hybrid nanowire [49, 52, 53]. Future work involving further growth and device measurements will aim to conclusively understand the properties of full-shell InAs/Pb hybrids, including the field-dependent behaviour [50].

5 Processing Pb coated InAs nanowires for devices

In this section we summarize the influence of standard clean room processing techniques on Pb films on InAs nanowires. First, we examined the effect on Pb-coated nanowires of immersion in isopropanol (60 s), acetone (15 min), methylisobutylketone:isopropanol 1:3 (90 s), n-methyl-2-pyrrolidone (NMP) (15 min), dioxolane (15 min) and H_2O (30 s). Using SEM imaging, we found that only H_2O visibly affected the Pb films, and in fact could be used as a selective etchant against InAs. Selective etching is demonstrated in Fig. S16, where we show an InAs/Pb nanowire before (**a**) and after (**b**) local exposure to H_2O for 10 s. Similar results are shown in Fig. S16 **c-d** for full-shell InAs/Pb nanowires. Using H_2O as our etchant obviates a prevalent problem in device fabrication, where perfectly selective etches are rare. For instance, the standard etch for Al against InAs may damage the underlying InAs[19]. The H_2O used throughout was purified MilliQ with resistivity $\rho > 15$ MΩ.

Processing for tunnel spectroscopy devices (Fig. 3 of the main text and Figs S11,S15) followed a 'self-aligned' procedure according to:

1. Nanowire transfer from growth substrate to device substrate using a micromanipulator under an optical microscope.

2. Source contact pattern exposed in poly-methyl-methacrylate (PMMA) resist using electron beam lithography.

3. Pattern developed in PMMA using methylisobutylketone:isopropanol 1:3.

4. Pb was etched in the source contact area by immersion in H_2O for 10 s.

5. The drain and gate pattern was exposed and developed in the same PMMA resist layer.

6. Ti/Au (5 nm/250 nm) was deposited using e-beam evaporation after in-situ Ar^+-milling, and lift-off in acetone produced the final contacts/gate pattern.

PMMA features an undercut profile after development, meaning the etch extends ~ 50 nm beyond the patterned area at the resist surface. In contrast, the area covered by Ti/Au is defined by the pattern at the resist surface. This 'self-alignment' feature ensured there was a ~ 50 nm-long bare InAs segment between the Ti/Au source contact and Pb film in e.g. Fig. S15 **b**. Processing for island devices (Fig. 4 of the main text and Figs S12,S13,S14) utilised a similar procedure. However, *all* contacts were defined in the same lithography step at step 2, since Pb was etched underneath both source and drain. As step 5 was rendered unnecessary it was omitted.

Since these microscopic Pb films react with H_2O, samples and devices were stored in vacuum as much as possible to avoid exposure to ambient moisture. However, the clear observation of hard-gap superconductivity in devices and the epitaxial crystal structure seen from TEM on nanowires exposed for up to 24 hours in air, indicates that the Pb

films are resilient to a degree of exposure that does not strongly impact their practical use. Additionally, depositing a capping layer of, e.g., Al or AlOx would likely prevent any oxidation/degradation.

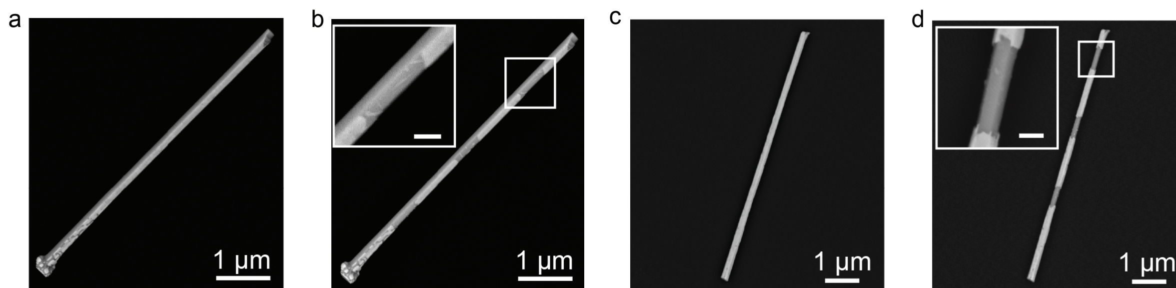

Figure S16: **Etching of Pb films with H_2O.** SEM micrographs of an InAs nanowire with a 10 nm Pb half-shell before (**a**) and after (**b**) exposure to H_2O for 10 s. InAs nanowire with a 20 nm Pb full-shell before (**c**) and after (**d**) exposure to H_2O for 25 s. Inset scale bars are 200 nm.

As discussed in section 1.2, Pb films dewet at elevated temperatures. We tested this in a controlled manner by heating InAs/Pb nanowires inside a TEM using a temperature controlled sample holder. We found that the Pb films spontaneously dewet for $T \sim 100°C$. Consequently, thin Pb films may dewet during e.g. resist baking at $T \sim 100°C$. Throughout, we evaporated the anisole solvent present in our PMMA resists by placing them under moderate vacuum for one hour.

Finally, we use Ar^+ RF-milling immediately prior to Ti/Au contact deposition to ensure low-resistance ohmic contacts to InAs nanowires. However, we found that on some devices, the Pb film was damaged by our standard procedure of 8 min milling under 18 mTorr pressure and 15 kW power. Although processing for all presented devices used this standard procedure, we have subsequently found that reducing the time to 3 min strongly limited this damage and preserves the integrity of the Pb films.

References

1. Vesselinov, M. I. *Crystal Growth for Beginners: Fundamentals of Nucleation, Crystal Growth and Epitaxy* (World Scientific, 2016).
2. Bjergfelt, M. *et al.* Superconducting Vanadium/Indium-Arsenide Hybrid Nanowires. *Nanotechnology* **30,** 294005 (2019).
3. Krogstrup, P. *et al.* Epitaxy of Semiconductor–Superconductor Nanowires. *Nature Materials* **14,** 400 (2015).
4. Wagendristel, A. & Wang, Y. *An Introduction to Physics and Technology of Thin Films* (World Scientific, 1994).
5. Antczak, G. & Ehrlich, G. *Surface Diffusion: Metals, Metal Atoms, and Clusters* (Cambridge University Press, 2010).

6. Reichelt, K. Nucleation and Growth of Thin Films. *Vacuum* **38,** 1083–1099 (1988).
7. Mehrer, H. *Diffusion in Solids: Fundamentals, Methods, Materials, Diffusion-controlled Processes* (Springer Science & Business Media, 2007).
8. Ring, T. A. Nano-sized Cluster Nucleation. *Advances in Colloid and Interface Science* **91,** 473–499 (2001).
9. Pentcheva, R. *et al.* Non-Arrhenius Behavior of the Island Density in Metal Heteroepitaxy: Co on Cu (001). *Physical Review Letters* **90,** 076101 (2003).
10. Venables, J. A. in *The Chemical Physics of Solid Surfaces* 1–45 (Elsevier, 1997).
11. Unal, B. *et al.* Nucleation and Growth of Ag Islands on fivefold Al-Pd-Mn quasicrystal Surfaces: Dependence of Island Density on Temperature and Flux. *Physical Review B* **75,** 064205 (2007).
12. Janssens, K. G. *et al.* Computing the Mobility of Grain Boundaries. *Nature Materials* **5,** 124 (2006).
13. Basu, I., Chen, M., Loeck, M., Al-Samman, T. & Molodov, D. Determination of Grain Boundary Mobility during Recrystallization by Statistical Evaluation of Electron Backscatter Diffraction Measurements. *Materials Characterization* **117,** 99–112 (2016).
14. Molodov, D., Shvindlerman, L. & Gottstein, G. Impact of Grain Boundary Character on Grain Boundary Kinetics. *Zeitschrift für Metallkunde* **94,** 1117–1126 (2003).
15. Anthony, T. R. Grain-driven Zone Melting. *Journal of Applied Physics* **56,** 477–485 (1984).
16. Mikkelsen, A. E. G., Kotetes, P., Krogstrup, P. & Flensberg, K. Hybridization at Superconductor-Semiconductor Interfaces. *Physical Review X* **8,** 031040 (July 2018).
17. Gül, Ö. *et al.* Hard superconducting gap in InSb nanowires. *Nano Letters* **17,** 2690–2696 (2017).
18. Pendharkar, M. *et al.* Parity-Preserving and Magnetic Field Resilient Superconductivity in Indium Antimonide Nanowires with Tin Shells. Preprint at http://arxiv.org/abs/1912.06071 (Dec. 2019).
19. Carrad, D. J. *et al.* Shadow Lithography for In-Situ Growth of Generic Semiconductor/Superconductor Devices. Preprint at http://arxiv.org/abs/1911.00460 (Nov. 2019).
20. Tran, R. *et al.* Surface Energies of Elemental Crystals. *Scientific Data* **3,** 160080 (2016).
21. Matthias, B. T., Geballe, T. H. & Compton, V. B. Superconductivity. *Reviews of Modern Physics* **35,** 1 (1963).
22. Dryzek, J. & Wróbel, M. Observation of the Recrystallization Process in Pure Nb and Zr Using Positron Lifetime Spectroscopy and XRD Techniques. *Physica Status Solidi (b)* **255,** 1800051 (2018).
23. Eisenstein, J. Superconducting Elements. *Reviews of Modern Physics* **26,** 277 (1954).
24. Kostorz, G., Isaacs, L., Panosh, R. & Koch, C. Anisotropy of the Upper Critical Field of Superconducting Technetium. *Physical Review Letters* **27,** 304 (1971).

25. Sekula, S., Kernohan, R. & Love, G. Superconducting Properties of Technetium. *Physical Review* **155,** 364 (1967).

26. Humphreys, F., Rohrer, G. & Rollett, A. in *Recrystallization and Related Annealing Phenomena* 121–167 (Elsevier Oxford, 2004).

27. Yu, J. M. Surface Self-Diffusion of Vanadium (1980).

28. Wexler, A. & Corak, W. S. Superconductivity of Vanadium. *Physical Review* **85,** 85 (1952).

29. Sekula, S. & Kernohan, R. Magnetic Properties of Superconducting Vanadium. *Physical Review B* **5,** 904 (1972).

30. Löptien, P., Zhou, L., Khajetoorians, A., Wiebe, J. & Wiesendanger, R. Superconductivity of Lanthanum Revisited: Enhanced Critical Temperature in the Clean Limit. *Journal of Physics: Condensed Matter* **26,** 425703 (2014).

31. Satta, A., Willaime, F. & de Gironcoli, S. First-Principles Study of Vacancy Formation and Migration Energies in Tantalum. *Physical Review B* **60,** 7001 (1999).

32. Brownlee, L. Lattice Constant of Grey Tin. *Nature* **166,** 482 (1950).

33. Molodov, D., Swiderski, J., Gottstein, G., Lojkowski, W. & Shvindlerman, L. Effect of Pressure on Grain Boundary Migration in Aluminium Bicrystals. *Acta Metallurgica et Materialia* **42,** 3397–3407 (1994).

34. Van Gurp, G., De Waard, P. & Du Chatenier, F. Thermomigration in Indium Films. *Applied physics letters* **45,** 1054–1056 (1984).

35. Jelver, L., Larsen, P. M., Stradi, D., Stokbro, K. & Jacobsen, K. W. Determination of Low-Strain Interfaces via Geometric Matching. *Physical Review B* **96,** 085306 (2017).

36. Sestoft, J. E. *et al.* Engineering Hybrid Epitaxial InAsSb/Al Nanowires for Stronger Topological Protection. *Physical Review Materials* **2,** 044202 (2018).

37. Gazibegovic, S. *et al.* Epitaxy of Advanced Nanowire Quantum Devices. *Nature* **548,** 434–438 (2017).

38. Yang, Z.-x. *et al.* Surfactant-Assisted Chemical Vapour Deposition of High-Performance Small-Diameter GaSb Nanowires. *Nature Communications* **5,** 1–10 (2014).

39. Momma, K. & Izumi, F. VESTA 3 for Three-Dimensional Visualization of Crystal, Volumetric and Morphology Data. *Journal of Applied Crystallography* **44,** 1272–1276 (2011).

40. Giannuzzi, L. A. & Stevie, F. A. A Review of Focused Ion Beam Milling Techniques for TEM Specimen Preparation. *Micron* **30,** 197–204 (1999).

41. Krizek, F. *et al.* Growth of InAs Wurtzite Nanocrosses from Hexagonal and Cubic Basis. *Nano Letters* **17,** 6090–6096 (2017).

42. Nalwa, H. S. *Handbook of Thin Films, Five-Volume Set* (Elsevier, 2001).

43. Paajaste, J. *et al.* Pb/InAs Nanowire Josephson Junction with High Critical Current and Magnetic Flux Focusing. *Nano letters* **15,** 1803–1808 (2015).

44. Chang, W. *et al.* Hard Gap in Epitaxial Semiconductor–Superconductor Nanowires. *Nature Nanotechnology* **10,** 232 (2015).

45. Albrecht, S. M. *et al.* Exponential Protection of Zero Modes in Majorana Islands. *Nature* **531,** 206 (2016).

46. Albrecht, S. *et al.* Transport Signatures of Quasiparticle Poisoning in a Majorana Island. *Physical Review Letters* **118,** 137701 (2017).

47. Vaitiekėnas, S. *et al.* Selective-Area-Grown Semiconductor-Superconductor Hybrids: A Basis for Topological Networks. *Physical Review Letters* **121,** 147701 (Oct. 2018).

48. Shen, J. *et al.* Parity Transitions in the Superconducting Ground State of Hybrid InSb-Al Coulomb Islands. *Nature Communications* **9,** 4801 (Nov. 2018).

49. Vaitiekėnas, S., Deng, M.-T., Nygård, J., Krogstrup, P. & Marcus, C. M. Effective g-Factor of Subgap States in Hybrid Nanowires. *Physical Review Letters* **121,** 037703 (July 2018).

50. Vaitiekėnas, S., Deng, M.-T., Krogstrup, P. & Marcus, C. M. Flux-Induced Majorana Modes in Full-Shell Nanowires. Preprint at http://arxiv.org/abs/1809.05513 (Sept. 2018).

51. Lee, E. J. H. *et al.* Spin-Resolved Andreev Levels and Parity Crossings in Hybrid Superconductor-Semiconductor Nanostructures. *Nature Nanotechnology* **9,** 79–84. ISSN: 1748-3387 (Jan. 2014).

52. Deng, M. *et al.* Majorana Bound State in a Coupled Quantum-dot Hybrid-Nanowire System. *Science* **354,** 1557–1562 (2016).

53. Prada, E. *et al.* From Andreev to Majorana Bound States in Hybrid Superconductor-Semiconductor Nanowires, Preprint at http://arxiv.org/abs/1911.04512 (Nov. 2019).

54. Zhang, H. *et al.* Ballistic Superconductivity in Semiconductor Nanowires. *Nature Communications* **8,** 16025. ISSN: 2041-1723 (July 2017).